We are IntechOpen, the world's leading publisher of Open Access books Built by scientists, for scientists

4,800
Open access books available

122,000
International authors and editors

135M
Downloads

Our authors are among the

154
Countries delivered to

TOP 1%
most cited scientists

12.2%
Contributors from top 500 universities

WEB OF SCIENCE™

Selection of our books indexed in the Book Citation Index in Web of Science™ Core Collection (BKCI)

Interested in publishing with us?
Contact book.department@intechopen.com

Numbers displayed above are based on latest data collected.
For more information visit www.intechopen.com

1

Conventional Transmission Electron Microscope Observation of Electric and Magnetic Fields

Katsuhiro Sasaki[1], Hidekazu Murata[2], Kotaro Kuroda[1] and Hiroyasu Saka[1]
[1]*Department of Quantum Engineering, School of Engineering, Nagoya University,*
[2]*Department of Electrical and Electronic Engineering, Meijyo University,*
Japan

1. Introduction

Transmission electron microscopy (TEM) has played an increasingly important role in the successful development of the micro-electronics industry by characterizing electric and/or magnetic device structures with decreasing dimensions. In particular, characterizing the dynamic behavior of electric and magnetic fields within and surrounding a device is important to understand and control its properties (Wang et al., 2004).

Two well-known methods have been used to observe the electric and magnetic field distribution in a TEM. The first one is electron holography (Tonomura, 1987), which requires a highly coherent electron source and an extensively modified transmission electron microscope. Though electron holograph gives a quantitative measurement of electromagnetic potential, it offers only a limited view due to the limitation of the width of the interference region between the object and the reference wave.

The other one is Lorentz microscopy. Though this method can be performed in a conventional TEM, the image in Fresnel mode is obtained in defocused condition and, the image in Foucault mode is not suitable for quantitative analysis (Cohen, 1968; Fisher and Blades, 1972; Chapman, 1984). Some efforts have been made to extract quantitative results from Lorentz images, for example, the transport intensity equation (TIE) approach by Bajit et al. (2000) and, Graef and Zhu (2001). However, this approach requires post image processing to form the images representing the electric or magnetic fields.

There is the third method called the shadow method that was developed in the early days of the development of transmission electron microscopy (Marton and Lachenbruch, 1949; Blackman and Grunbaum, 1957; Jakubovics, 1964; Lazzari et al., 1971; Keyser, et al., 1975; Wade, 1976). However, the development of this method has been suspended and neglected compared to the rapid development of the other two methods.

In our previous work (Sasaki, et al, 2000, 2003) on in-situ electron holography experiments, we found a similar phenomenon, that is the distortion of the shadow image of the selected area diffraction (SAD) aperture while applying an external electric potential to the specimen. In the experiment, the observation was performed in very low magnification mode, called

"Low Mag" mode (hereinafter referred to as "LM" mode). As a practical method of rough alignment of the beam tilt in the LM mode, the shadow image of the SAD aperture was observed. The specimen is a tip of GaP Light Emitting Diode (LED), whose shape observed in a focused ion beam microscope is shown in Fig. 1a. The schematic view of the specimen and the geometrical relationship of the electron beam, when it is observed in a TEM, is shown in Fig. 1b. During the alignment procedure, as shown in the LM mode images in the TEM (Fig. 2), a local distortion of the edge shape of the SAD aperture near the reverse biased p-n junction of the specimen was observed that did not affect the image of the specimen at all. The continuous circular edge shape of the aperture was observed when there was no external voltage, and when a forward bias was applied as shown in Fig. 2a and b, respectively. However, a discontinuity in the edge shape appeared when reverse bias was applied as shown in Fig. 2c and d. This distortion increased with increasing applied voltage as shown in the superimposed schematic drawing of the images in Fig. 2e.

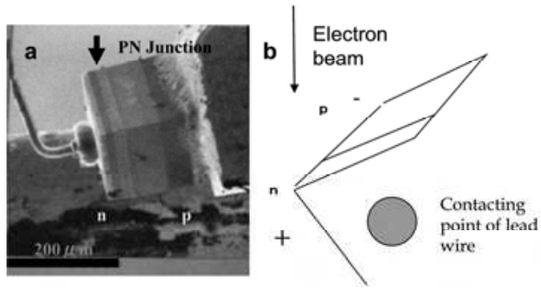

Fig. 1. A scanning ion microscope (SIM) image (a) and the schematic drawing (b) of the GaP LED chip. The arrow indicates the direction of the electron beam when the specimen is observed in a TEM.

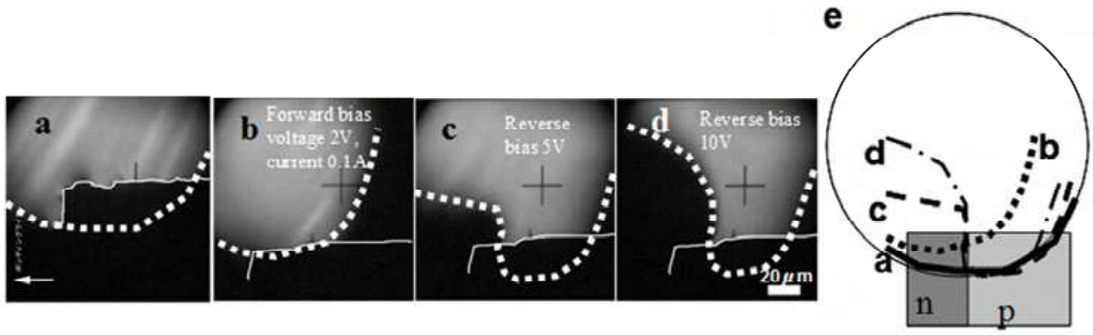

Fig. 2. Low magnification image of GaP chip and the shadow image distortion of the SAD aperture at (a) 0 V, (b) 2 V of forward, (c) 5 V and (d) 10 V of reverse bias. (e) the superimposed schematic drawing of the shadow images of the aperture.

In the above mentioned work, we discussed the geometrical optics for this phenomenon and found that the distortion of the shadow image of the SAD aperture was proportional to the deflection of the electron beam by the electric field around the position of the specimen (Sasaki and Saka, 2005; Sasaki, et. al. 2006). We also suggested that quantitative measurement not only of electric fields but also magnetic fields could be accomplished using this phenomenon. Analogous to electron optics, our method can be viewed as a shadow method (Marton and Lachenbruch, 1949; Jakubovics, 1964; Wade , 1976). However, our method, and the benefit

thereof, is applicable in a modern conventional TEM without extensive modification. We call our method, temporally, the shadow image distortion (SID) method.

In this chapter, we will discuss further details of the geometrical electron optics in this phenomenon and the method for determining the optical parameters of a TEM system, which are important for observing the electric and/or magnetic fields using this phenomenon. Some examples of applications which demonstrate the quantitative measurement of the electric field using our method are introduced.

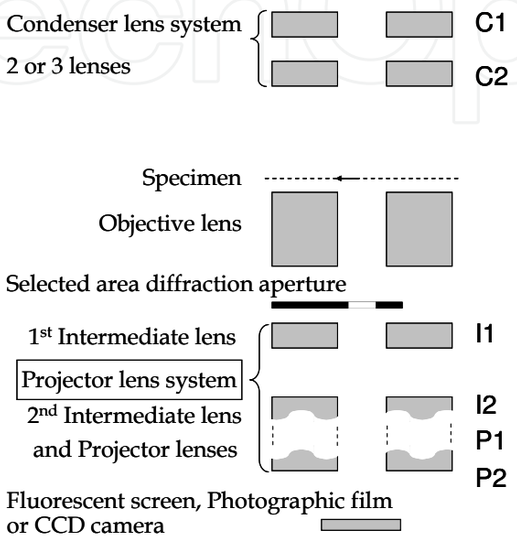

Fig. 3. Typical lens system of a conventional TEM.

2. Geometrical optics analysis of shadow image distortion

A conventional TEM consists of three lens systems as shown in Fig. 3. The first is the condenser lens system which focuses the electrons coming from the electron gun and illuminates the specimen. The second is the objective lens which, in ordinary mode, forms the image of the specimen for the following lens system. The third is the projector lens system which projects the enlarged specimen image onto the fluorescent screen, the photographic film or, contemporary, charge coupled device (CCD) camera. For example, in the H-9000NAR (Hitachi High Technologies, Tokyo, Japan) used in our work, the condenser lens system consisted of two lenses, i.e., C1 and C2, and the projector lens system consisted of four lenses, i.e., two intermediate lenses, i.e., I1 and I2, and two projector lenses, i.e., P1 and P2. We consider the behavior of the lenses, which are the condenser lens C2, the objective lens and the intermediate lens I1, to analyze the movement of the shadow image of the beam obstructer placed at the position of the SAD aperture that is between the objective lens and intermediate lens I1.

In the LM mode, the image of the specimen is formed by the intermediate lens, and the condenser lens system locates the electron beam onto the specimen for illumination. The objective lens which has a lesser effective part in this mode is usually turned off or only weakly activated. As mentioned above, we consider one condenser lens C2 as a condenser lens system, objective lens and first intermediate lens I1 only, which are shown in the ray diagram of the electron microscope in Fig. 4.

First of all, we consider the simplest condition in which an ideal parallel beam illuminates the specimen when the objective lens is turned off (Fig. 4a). Then the behavior of C2 condenser lens is taken into account. In the second condition, the objective lens is completely turned off in the divergent beam illumination (Fig. 4b). In the third condition, the objective lens is weakly activated in the parallel beam illumination (Fig. 4c). We found that the objective lens does not affect the imaging of the specimen. However, it can control the sensitivity of the field detection. In this last case, which can be performed in a real operation, the objective lens is weakly activated in the divergent beam illumination (Fig. 5).

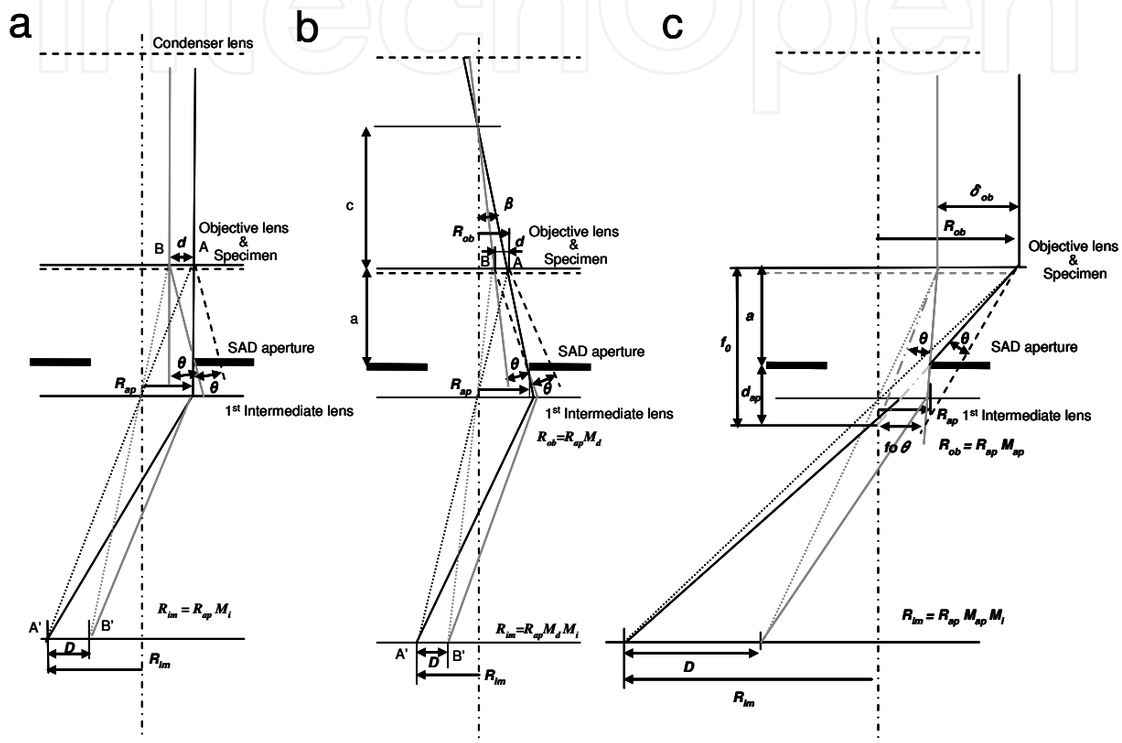

Fig. 4. Ray diagrams of (a) 1st, (b) 2nd and (c) 3rd condition.

The ray diagram in the first condition is shown in Fig. 4a. The SAD aperture is located between the specimen and the intermediate lens. Here we assume that the divergence of the electron beam is relatively small, for example on the order of 10^{-4} rad. In the parallel beam illumination, the shadow image of the SAD aperture (R_{ap} in radius) is projected onto the image plane with a radius $R_{im} = R_{ap} M_i$, where M_i is the magnification of the intermediate lens. When the electron beam is deflected by the electric field of the specimen at an angle θ, the electron beam from the specimen between A and B is obstructed by the SAD aperture. The electron beam obstructed by the SAD aperture has been imaged between A' and B' on the image plane of the intermediate lens. This means that the edge of the shadow image of the SAD aperture will move from A' to B'. This is observed as a shift of the aperture edge in the image. The distance of A-B, i.e. d, can be calculated by the deflection angle θ and the distance a between the SAD aperture and the specimen. The distance d will be enlarged by the intermediate lens to $D = a\ \theta\ M_i$ at the image plane and then enlarged or reduced to be imaged on the fluorescence screen by the following lens system with a magnification M_p (Sasaki and Saka, 2005).

In the TEM that we usually used, the condenser lens system focused the electron beam once before the specimen, then illuminated the specimen with a certain divergence angle of electron beam as shown in the ray diagram in Fig. 4b. In the second condition, we take into account the divergence of the beam due to the condenser lens (Sasaki et al., 2008a). In this condition, the beam direction has a different vector as a function of distance from the optical axis of the electron microscope. The angle β between the optical axis and electron beam direction will be $\beta=r/c$, where r is the distance from the optical axis and c is the distance from the specimen surface to the focal point of the electron beam. Though the electron beam has a divergence angle, the image is formed at the same position on the image plane of the intermediate lens in the magnification M_i as shown in the Fig. 4b. However, the area on the specimen that corresponds to the area where the electron beam can pass through the SAD aperture with radius R_{ap} is reduced due to the electron beam divergence. The radius R_{ob} of the area on the specimen plane that corresponds to the area on the SAD aperture plane with radius R_{ap} is written as $R_{ob} = R_{ap}\, c/(a+c)$. Namely, the radius of the shadow image of the SAD aperture will be reduced by magnification M_d, where $M_d = c/(a+c)$. When the electron beam is deflected by the electric field of the specimen at an angle θ, the electron beam at the edge of the SAD aperture is shifted $a\ \theta$ and obstructed by the SAD aperture. The shift $a\ \theta$ on the aperture plane corresponding to the distance A and B on the specimen plane will be reduced to $a\ \theta\ M_d$ where this corresponds to the image between A' and B'. The distance between A' and B' which corresponds to the shift of the edge of the shadow image of aperture D is calculated to be $D = a\ \theta\ M_d\ M_i$ with M_i the magnification of the intermediate lens. This result indicates that the shift of the shadow image of the SAD aperture is reduced by M_d using the electron beam with the divergence angle.

In the third condition, particularly, of the H-9000 NAR, the objective lens is weakly activated in the LM mode. The ray diagram in this condition is shown in Fig. 4c. In the LM mode with the weakly activated objective lens, the back focal plane of the objective lens is located slightly lower than the front focal plane of the intermediate lens. For simplicity, the objective lens plane is considered to be approximately in the plane of the specimen, because a very low current is applied to the objective lens as for example, in the case of H-9000 NAR, the current is one twentieth of the ordinary imaging mode, then it will work as a transfer lens and does not affect the image formation of the lens which has the object plane at the specimen position. Then we consider a parallel beam condition again to discuss the effect of the objective lens in the geometrical optics. When the objective lens is in the same plane as the specimen, the image of the specimen is formed at the same magnification as if there was no objective lens. However, the electron beam passing through the specimen will be focused to one point on the back focal plane of the objective lens and then diverge. The area on the specimen through which the electrons pass, and then pass through the SAD aperture hole with radius R_{ap} is the reverse projection of the SAD aperture on the specimen plane with radius R_{ob} as indicated by the arrows in Fig. 4c. The radius R_{ob} is calculated to be $R_{ob} = R_{ap}\, f_o\ /\ d_{ap}$, where R_{ap} is the radius of the SAD aperture, f_o is the focal length of the objective lens and d_{ap} is the distance between the back focal plane of the objective lens and the SAD aperture. The shadow image radius R_{im} of the SAD aperture in the image plane of the intermediate lens is the magnified image of this reverse projection by the intermediate lens; it is given by: $R_{im} = R_{ap}\, M_{ap}\, M_i$, where M_{ap} is $f_o\ /\ d_{ap}$.

When the electron beam is deflected by the electric field at an angle θ, the focal point of the electron beam on the back focal plane of the objective lens is displaced by $f_o\ \theta$. On the surface of the specimen, the area on the specimen through which pass the electrons passing through

the SAD aperture hole will be changed. The shift of the aperture edge δ_{ob} is calculated to be $\delta_{ob} = f_o\ \theta\ a\ /\ d_{ap}$. The shift δ_{ob} is enlarged onto the image plane of the intermediate lens with magnification M_i. Thus the shift of the aperture edge D is calculated as $D = a\ \theta\ M_{ap}\ M_i$.

In the forth condition, that could be obtained in real operating conditions, the optics will be divided into two cases, i.e., whether the relations of the length between c and f_o are either $c > f_o$ or $c < f_o$.

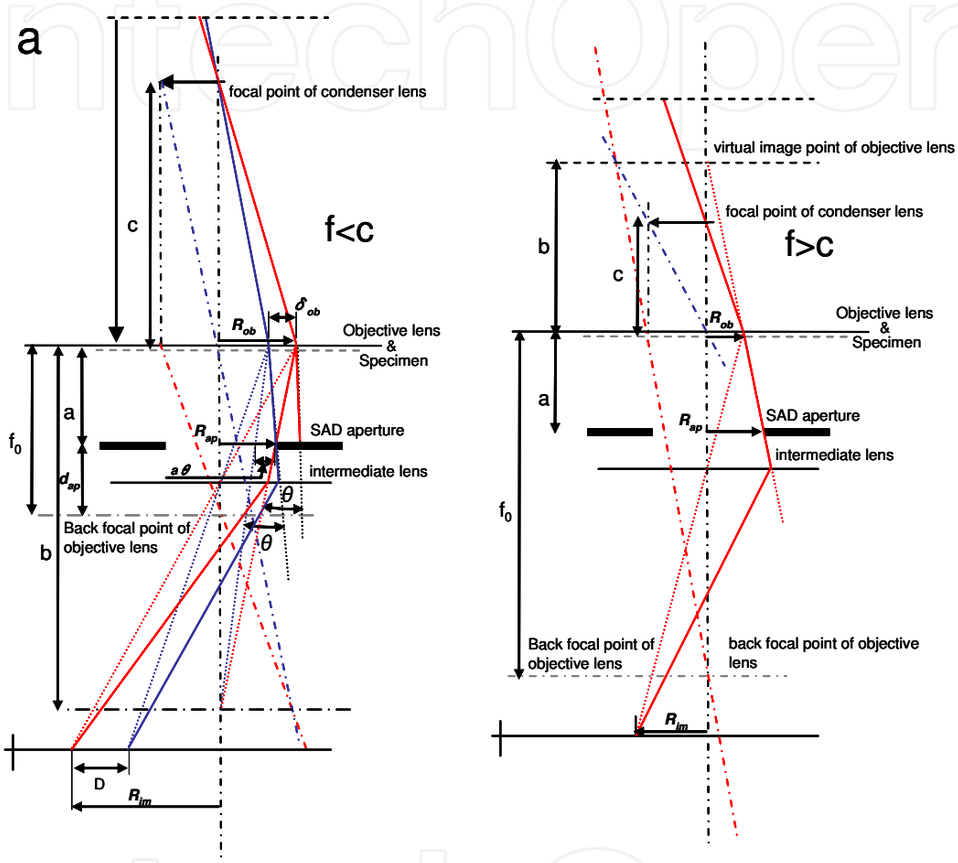

Fig. 5. Ray diagrams of 4th condition in (a) f<c and (b) f>c.

If $c > f_o$, as shown in Fig. 5a, the electron beam diverges from the focal point of the condenser lens and is focused again at the image plane of the objective lens at b. The length b can be calculated from the relation $1/b + 1/c = 1/f_o$, where c is the distance between the focal point of the electron beam after the condenser lens and the position of the objective lens, then b can be rewritten to be $f_o\ c/(c - f_o)$. The area on the specimen through which pass the electrons, passing through the SAD aperture hole is, again, the reverse projection of the SAD aperture on the specimen plane. The radius R_{ob} of the reverse projected SAD aperture is calculated as $R_{ob} = R_{ap}\ b/\ (b - a)$ in this case, where R_{ap} is the radius of the SAD aperture, a is the distance between the specimen and/or objective lens, and the SAD aperture. Replacing $f_o c/(c - f_o)$ into b gives

$$R_{ob}\ /\ R_{ap} = f_o c\ /\left[f_o\left(a + c\right) - ac \right]$$

M_d and M_{ap} can be written as $c/(a + c)$ and $f_o/(f_o - a)$, respectively. Rewriting R_{ob}/R_{ap} with M_d and M_{ap} gives

$$R_{ob} / R_{ap} = M_d M_{ap} / \left(M_d + M_{ap} - M_d M_{ap} \right)$$

Analogous to the above mentioned discussion in the third condition gives

$$D = a\theta M_d M_{ap} M_p M_i / \left(M_d + M_{ap} - M_d M_{ap} \right) \quad (2.1)$$

In the second case, $c < f_o$, the focal point of the condenser lens can be assumed to be the virtual image at the position $-b$, which is the object plane of the weakly activated objective lens. The length b can be calculated from the relation $1/c = 1/f_o + 1/b$ in this case, then b can be rewritten to be $f_o c/(f_o - c)$. The radius R_{ob} of the reverse projected SAD aperture is calculated as $R_{ob} = R_{ap}\, b/(b+a)$ in the latter case. Replacing $f_o c/(f_o - c)$ into b, gives $R_{ob}/R_{ap} = f_o c/[f_o(a + c) - ac]$. This result gives the same equation as (2.1).

If M_{ap} is nearly equal to unity, the above equation can be simplified to

$$D = a\theta M_d M_{ap} M_p M_i \quad (2.2)$$

As discussed above, the results show that the displacement D of the shadow image of the beam obstructer, which is placed at the position of the SAD aperture, will be proportional to the deflection angle θ of the electron beam at the position of the specimen. The differences in the deflection angle θ at different positions on the specimen causes different displacements of the shadow, which forms the distortion of the shadow image of the beam obstructer placed at the position of the SAD aperture (hereinafter referred to as the "shadow aperture").

3. Experimental confirmation of geometrical optics analysis

3.1 Measurement of optical parameters of the magnetic lens system in a TEM

As discussed in section 2, several magnification parameters, i.e., M_d, M_{ap}, M_p and M_i, play an important role in measuring the electric and/or magnetic field of the specimen in the optical system of the TEM. In order to confirm the above mentioned geometrical electron optics analysis and measure the optical parameters, we performed the following experiments.

The electron microscopy observation was done in a TEM H-9000NAR equipped with an ordinary LaB_6 thermal emission electron gun at an accelerating voltage of 300 kV. The observation was performed in the LM mode.

Uniformly shaped lattice grids of known size were simultaneously placed at the position of the specimen and the SAD as the shadow aperture. The magnification of the shadow image of the grid placed at the same position as the SAD aperture was compared to the magnification of the image of the specimen allowing evaluation of the optical parameters.

Three types of lattice shaped grids were employed as the specimen and the shadow aperture in this experiment. The first is the Nickel screen mesh with spacing of 16.94 μm. The second is the holey carbon films (Quantifoil R2/2: Quantifoil Micro Tools GmbH, Jena, Germany)

with holes of 2 μm diameter arranged in a square lattice pattern with edge-to-edge spacing of 4 μm. The third is the square lattice on a gold thin foil with thickness 10 μm fixed to a 100 mesh Cu grid, which was formed in the shape of a square lattice with 1 μm x 1 μm square holes with lattice spacing of 2.46 μm by using Focused Ion Beam (FIB) apparatus FB-2000 (Hitachi High Technologies, Tokyo, Japan).

In order to evaluate the optical parameters M_d, M_{ap}, M_p and M_i, the Nickel screen mesh or Quantifoil R2/2 was used. Figure 6 shows an example of the image and shadow image when the Quantifoil R2/2 was used, in which the holes in the carbon film with same as size in 2 μm diameter, were observed in different diameter.

First of all, the magnification of the specimen image, the value of $M_p \times M_i$ was determined directly on the photographic film. We used the standard setting of the projector lens system of the microscope with zero objective lens current, which corresponds to the 1st and 2nd condition discussed in section 2, therefore giving the optical parameter M_{ap} as unity. The magnifications of the condition assigned to 0.2 K, 0.3 K and 0.5 K of LM mode was 230, 320 and 586 with the zero objective lens current, respectively.

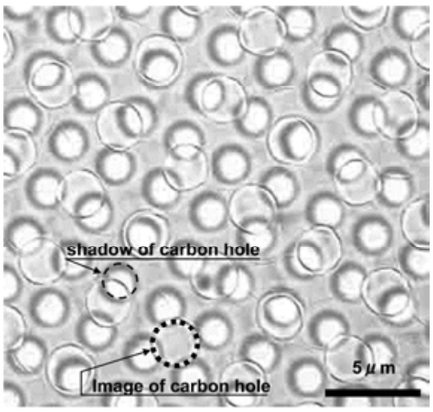

Fig. 6. Observed image and shadow image of Quantifoil 2/2.

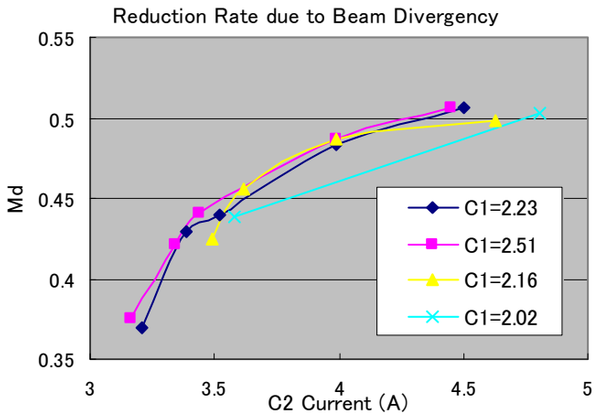

Fig. 7. Measured M_d as a function of C2 condenser lens current at different C1 condenser lens currents.

Figure 7 shows the ratio of the distance between the holes on the image and shadow image as a function of the current I_{c2} which was applied to the C2 condenser lens when the

objective lens was turned off. Some data were obtained using the lattice of the Nickel screen mesh and others using the holes of Quantifoil R2/2. The results correspond to the value of M_d, which showed an initial rapid increase and gradual saturation as a function of the current applied to the C2 condenser lens. The measurements were taken at different currents applied to the first condenser lens C1. However, the results show that the current applied to C1 does not affect the value of M_d. This result supports our optical model which states that only C2 is appropriate to understanding our optical system.

As shown in Fig. 4b, M_d can be written as $c/(c+a)$. where a is the geometrically determined constant value. The value of c can be changed according to the focal length f_c of lens C2, which is determined as $c = L_{c\text{-}o} - f_c$, where $L_{c\text{-}o}$ is the distance between C2 and the objective lens. The focal length f_c of the magnetic lens is given as $f_c = k_c/I_{c2}^2$ (Liebmann 1955; Spence 1981), where I_{c2} is the current applied to lens C2 and k_c is the constant determined by the lens structure. Replacing c using $L_{c\text{-}o}$ and k_c/I_{c2}^2 gives

$$1 / M_d = 1 + a / (L_{c\text{-}o} - k_c / I_{c2}^{\,2})$$

Rewriting this equation gives

$$a M_d / (1 - M_d) = - k_c / I_{c2}^{\,2} + L_{c\text{-}o} \tag{3.1}$$

This result indicates that if the value of $a M_d/(1-M_d)$ is drawn as a function of $1/I_{c2}^2$, a liner relation will be given, and then k_c and $L_{c\text{-}o}$ can be given as the inverse slope and the y-intercept of the liner relation, respectively.

Figure 8 shows $a M_d/(1-M_d)$ as a function of $1/I_{c2}^2$ for C2 current between 3.42 and 4.45 A while keeping other lens conditions constant. The graph shows a liner relation and gives the value of k_c and $L_{c\text{-}o}$ to be 915 A²mm and 218 mm, respectively, where a is given as 155 mm on the blueprint of the microscope. This result indicates that the above geometrical optics analysis can explain the optical system in our microscope very well.

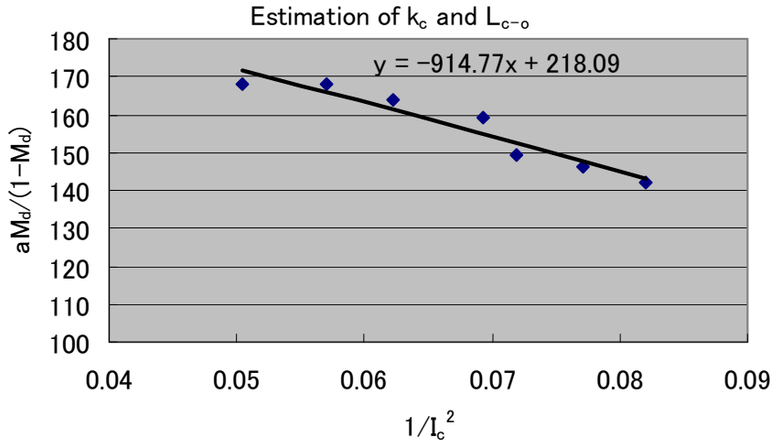

Fig. 8. Estimation of the distance between C2 and objective lens $L_{c\text{-}o}$ and the lens constant of objective lens k_c.

When current is applied to the objective lens, the parameter M_{ap} is not unity. The value M_{ap} might be estimated as a function of the objective lens current I_o. In real conditions in the

electron microscope, a completely parallel electron beam can not be obtained. Under this limitation, M_d can not to be unity. Therefore, the multiplied value of M_{ap} and M_d can be obtained as the ratio M_{dap} of the distance between the lattice on the image and the shadow image, which can be directly measured on the recorded image in the same way shown above, and will be a function of both M_{ap} and M_d. Regarding equation (2.1), M_{dap} could be written as

$$M_{dap} = M_d M_{ap} / \left(M_d + M_{ap} - M_d M_{ap} \right) \tag{3.2}$$

Replacing $M_{ap} = f_o / d_{ap} = f_o / (f_o - a)$ into (3.2), which is derived from the definition, gives

$$M_d / M_{dap} = f_o - M_d{}^a / f_o \tag{3.3}$$

The f_o can be written in the same way as for the case of f_c as $f_o = k_o / I_o{}^2$ where k_o is the constant of the objective lens. Placing this relation into equation (3.3) gives k_o as

$$k_o = a\, I_o{}^2 M_{dap} M_d / \left(M_{dap} - M_d \right) \tag{3.4}$$

The value of k_o plotted as a function of $I_o{}^2$ for several conditions (Fig. 9) gives a constant value of about 58 A²mm except at low I_o. For I_o less than 0.2 A, the difference between M_{dap} and M_d is lower by three orders of magnitude than the value of M_{dap} and M_d, which is less than the error in the measurement of M_{dap} and M_d. This is the reason why k_o is not constant at I_o less than 0.2 A. This result suggests that geometrical optics can explain the behavior of the electron microscope in our condition. As a result, all the parameters M_d, M_{ap} and $M_p \times M_i$ in equation (2.1) can be determined using the currents I_{c2} and I_o, which are those applied to the 2nd condenser and the objective lens, respectively.

Similar measurements have been performed in two types of high voltage electron microscopes (HVEM), H-1250ST (Hitachi High Technologies, Tokyo, Japan) and JEM-1000k RS (JEOL Ltd., Tokyo, Japan) as shown in Figs. 10 and 11. Both types of HVEM followed equations (3.1) and (3.4) very well, proving that our analysis can be applied to any type of TEM. Higher penetration power of a higher accelerating voltage will allow application of our method to observe the inside of materials.

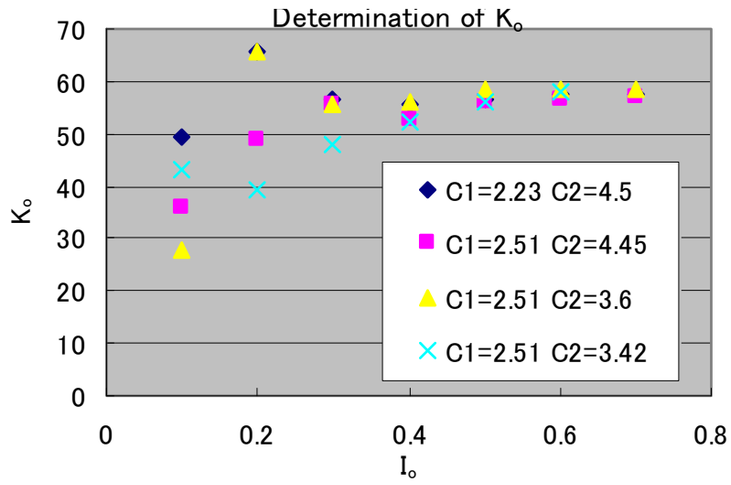

Fig. 9. Estimation of objective lens constant k_o

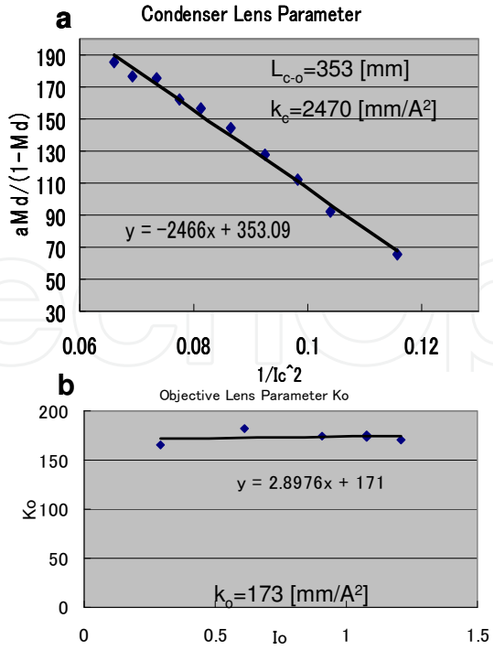

Fig. 10. The measurement of optical parameter (a) $L_{c\text{-}o}$ and k_c and (b) k_o of H-1250ST at an accelerating of 1000 kV.

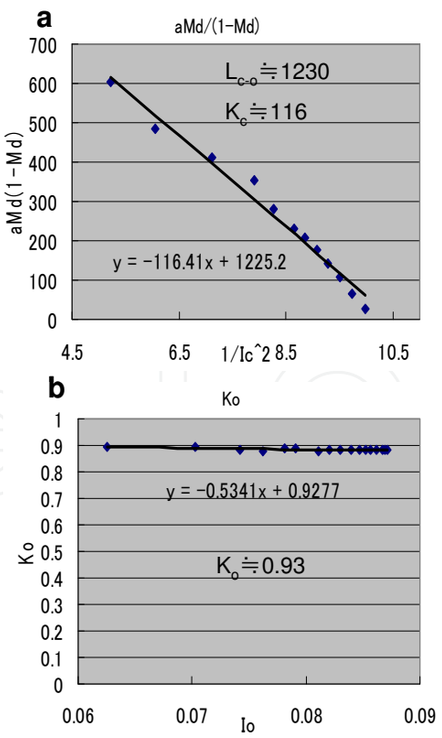

Fig. 11. The measurement of optical parameter (a) $L_{c\text{-}o}$ and k_c and (b) k_o of JEM-1000k RS at an accelerating of 1000 kV. The values are shown as the ratio of maximum current of the lenses.

3.2 Measurement of the shadow image shift in a uniform electric field

The amount and proportionality of the shadow image shift was examined by applying a uniform electric field to the electron beam with the electrodes placed at the specimen position as shown in Fig. 12. The specimen holder used in this experiment was the Kamino holder. The Kamino holder that was originally designed by Kamino and Saka (1993) as a heating holder has two electrodes where a heating element is usually fixed. One of the electrodes is connected to ground and the other electrode, through which the external voltage can be applied, is insulated from ground. In order to create a uniform electric field between the narrow gap of the two electrodes, a pair of electrodes consisting of Al plates with thickness of 13 μm were fixed to the respective electrodes of the specimen holder and carefully positioned with a spacing of 10 μm as shown in the optical microscope image and schematic drawing in Fig. 12a and b, respectively. The spacing between the electrodes was measured precisely on an electron micrograph to be 10.6 μm before the experiment.

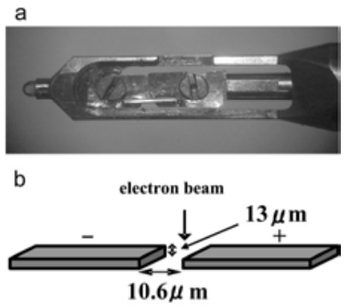

Fig. 12. The two electrodes fixed on the specimen holder (a) and the schematic drawing of them (b).

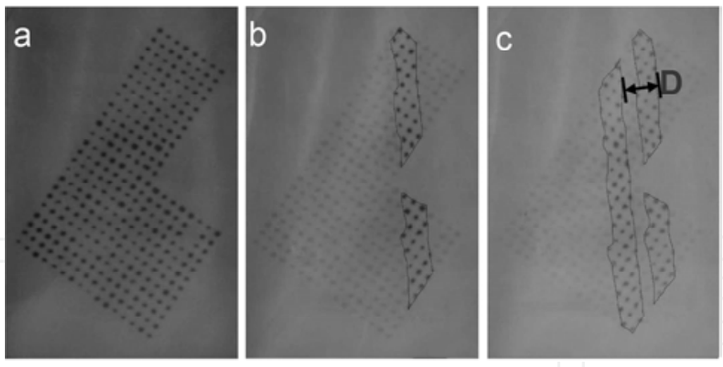

Fig. 13. The shadow image of (a) the FIB fabricated grid, (b) after the electrodes placed at the specimen position without applying voltage, i.e., 0 V, and (c) the shadow image applying 5 V with the superimposed image of 0 V. The shallow image of (a) is also superimposed on (b) and (c) as a guide of eyes.

The FIB fabricated grid as mentioned above was positioned at the SAD aperture as shown in Fig. 13a. This grid is well suited to avoiding misreading of the position in the repeated pattern because of minor irregularities in the shape caused by the unstable fabrication conditions during the home made fabrication processes. This type of shadow aperture was used to measure the shift of shadow image in a uniform electric field. The move of the shadow image

of the grid observed between the image of two electrodes (Fig. 13b and c) was recorded on TEM films as a function of the applied voltage between these two electrodes.

The shift of the shadow image of the FIB fabricated grid was measured up to 2 V on the fluorescence screen. The value of deflection of the electron beam calculated from the shift of the shadow image is shown as a function of applied field strength between the electrodes as shown in Fig. 14 for the condition a = 155 mm, $M_i \times M_p$=514, M_d=0.632, M_{ap}=1.57. Because the deflection angle θ of the electron beam is proportional to the integral of the x-y component of the electric field E along the length t of the electron passage at the specimen, the shift D of the aperture image is given by

$$D = kM_dM_{ap}M_iM_pEt \tag{3.5}$$

where k is the sensitivity coefficient.

Comparison of equations (2.2) and (3.5) gives,

$$\theta = k\,Et\,/\,a \tag{3.6}$$

In the uniform electric filed, the deflection angle of the electron is given by (Merli et al., 1975)

$$\theta = eEt\,/\,mv^2 \tag{3.7}$$

and in the case of magnetic field B is

$$\theta = eBt\,/\,mv^2$$

where e is the electron charge (1.602×10^{-19}C), and m and v are the relativistic mass and velocity of the electrons. Substituting equation (3.7) into (3.6) gives

$$k = ea\,/\,mv^2 \tag{3.8}$$

At an accelerating voltage of 300 kV, m=1.587×m$_0$, where m_0 is the rest mass of the electron, 9.109×10^{-31}kg and v=2.330×10^8m/s (Williams and Carter, 1996) gives k=3.06×10^{-7}m/V.

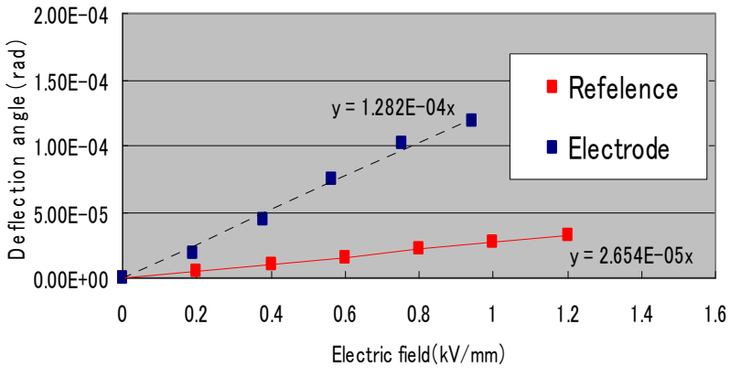

Fig. 14. The deflection angle of the electron beam as a function of applied electric field. The reference means the value when the field is restricted within the thickness of electrodes.

The experimental results showed good proportionality to the voltage applied to the electrodes. However, the discrepancy of *k* between the value derived from the equation (3.7) and the measured value was 4.8 times. In order to resolve this discrepancy, we will discuss the electric field distribution in our experiment, which in reality was not uniform and restricted to the gap between the two electrodes.

3.3 Numerical calculation of the electric field distribution along the electron trajectory

A numerical calculation has been performed to evaluate the distribution of the electric field around the two thin Al plate electrodes used in our experiments. An ordinary finite difference method was employed to calculate the 2D electric potential distribution on the cross section perpendicular to the edge of the electrodes and along the electron beam trajectory. The rectangular area of 2 mm and 1 mm was divided into 200 times 100 lattices with 10 μm mesh, and the potential $U_{x,y}$ on each lattices was calculated, where x=0 to 200 and y=0 to 100. The schematic drawing of the calculated lattice is shown in Fig. 15

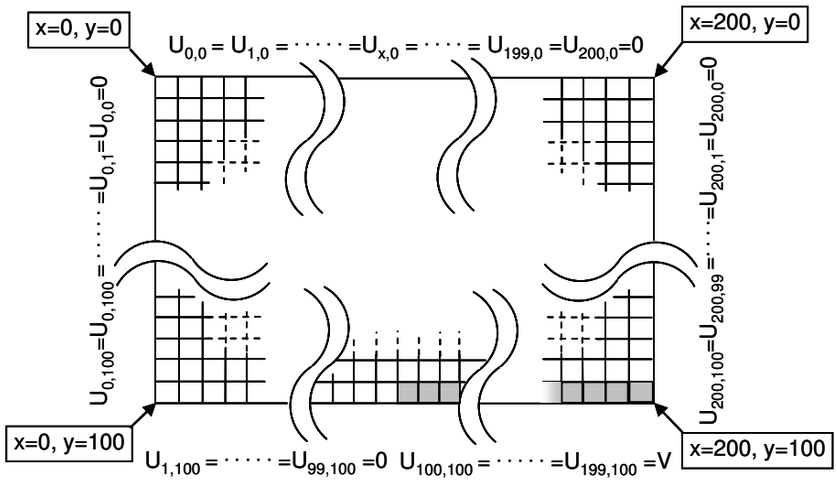

Fig. 15. The lattice model used for the estimation of the distribution of the field

The potentials on the boundaries were set on the top, i.e., $U_{x,0}$, and both side, i.e., $U_{0,y}$ and $U_{200,y}$, of the lattice at 0 Volt. The boundary values of the left bottom side in Fig. 15, which corresponds to the electrode connected to the ground earth, i.e., $U_{1,100}$ to $U_{99,100}$, were also set to 0 Volt. The boundary values of the right bottom side, i.e., between $U_{100,100}$ and $U_{199,100}$, were set to the applied voltages to the electrode. The difference equation on each lattice point was

$$U_{x,y} = \left(U_{x-1,y} + U_{x+1,y} + U_{x,y-1} + U_{x,y+1} \right) / 4$$

The matrix of $U_{x,y}$ for x=1 to 199 and y=1 to 99 were calculated using Gauss-Zeidelle method until the condition $\Sigma \Delta U_{xy} / \Sigma U_{xy} < 10^{-3}$ is satisfied.

Electric field was calculated taking the difference of adjacent potentials. The electron deflection was calculated from the integration of the field in the x-y plane assuming the trajectory of the electrons was along the Z axis during their passage through the field.

Figure 16a shows a schematic drawing of the calculated model around the electrodes using the finite differential method. The brighter contrast corresponds to higher potential in the calculation result in Fig. 16b. As shown in Fig. 16b, the potential of the electrodes diverged until about 0.5 mm away from the electrodes. Figure 16c shows the horizontal part of the electric field derived from the differentiation of the potential along the line running on the vertical centre of Fig. 16b, where the electron beam is running. The integral of the horizontal part of the electric field (Fig. 16d) giving a value 4.8 times of the value if the electric field is restricted to the thickness of the electrodes along the electron passage. This value corresponds to the difference of the sensitivity factor *k* between the experimental value and the calculated value using equation (3.8). This means that our observation is really measuring the deflection of the electron by this applied electric field.

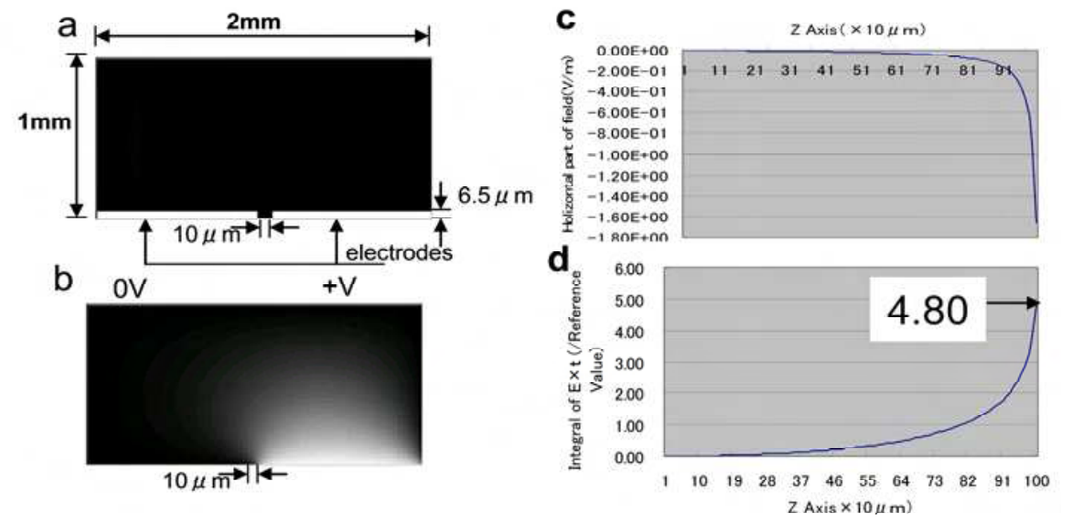

Fig. 16. The results of numerical calculation. (a) The schematic drawing of the calculated model and (b) gray scale map of the potential. (c) The horizontal part of electric field and (d) the integral along the line running vertical centre of (b).

We need the correction of the field distributed in the upper and lower part in which we are interested. However, this kind of problem could happen in the other method. For example, in the case of electron holography, the electromagnetic field is usually distributed over a wide area in and/or around the specimen whereas the interference region is limited to a bundle like shape. The reference electron wave will be affected by the electromagnetic field in the region that it is traversing, which is undetectable. The electric field observation in the previous work is just showing the difference between the region of interest and the region where no significant distribution of the field is assumed. However, our calculation revealed that the distribution of the field is hard to limit near the specimen and is usually distribute in the order of mm. The reliability of quantitative measurement will be discussed again in the next section.

4. Applications

The geometrical optics analysis and the measurement of a simple electric field showed us that the method we developed allow not only qualitative but also quantitative measurement

of electric and/or magnetic fields. In this section, we describe three examples of applications. Two of them are examples of qualitative measurement showing the facility of our method, and the other is an example of quantitative measurement.

As a preliminary experiment before the detailed experimental studies which use the electric field, we will show the magnetic field observation around a particle of commercially available ferrite magnet. Figure 17a shows the superimposed image of the specimen onto the shadow image of the Ni screen mesh when the specimen has not been inserted, i.e., without the distortion. An apparent distribution of the shadow image distortion was observed after the insertion of the specimen. In Fig. 17b, the magnetic line of force running perpendicular to the arrows indicates the direction and amount of shadow image shift. The figure demonstrates that the method can observe a magnetic field. In our method, the specimen is free from the magnetic field of the lens, because the objective lens is basically turned off or only weakly activated, which could be a benefit for the application of magnetic field observation.

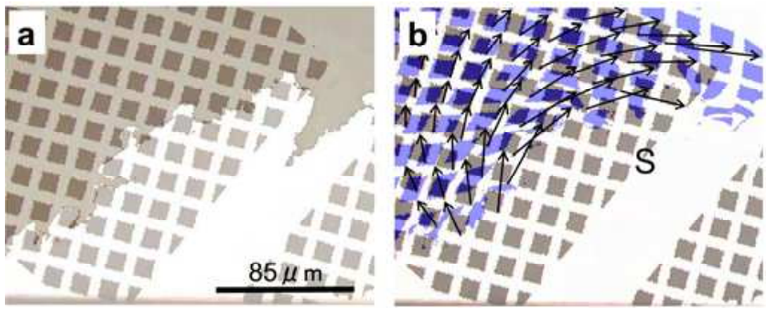

Fig. 17. The magnetic field observation of around a particle of commercially used ferrite magnet. (a) The superimposed image of the specimen and shadow image of the Ni screen mesh when the specimen has not been inserted. (b) The superimposition of the shadow images with the field (blue) onto without the field (gray). The arrows indicate the deflection of the electron beam. The magnetic line of force runs perpendicular to the arrows. The magnetic south pole of the particle marked by S.

In the following detailed experimental studies, we used the electric field only, because it was easy to create and control.

4.1 Qualitative measurement of a non-uniform electric field embedded in a uniform field

This example is the measurement of a non-uniform electric field embedded in a uniform field. The electric field far away from the electrodes will show a moderately changing feature with an average value compared to the field near the electrodes, which will show a rapid change. In order to observe the contribution of these two fields onto the shadow image, we prepared a specimen as shown in Fig. 18. Figure 18a is a schematic drawing of the specimen configuration. The half cut Cu grid with a carbon film is fixed to the electrode and a voltage applied to the counter electrode. As shown in Fig. 18b, the electric lines of force (the solid line arrows) and the electron beam trajectories (the red line arrows) are drawn, schematically, in the cross sectional view of the specimen. In the crescent of the metal, there will be a non-uniform rapidly changing field distribution. The electrodes supporting the Cu grid with the large gap will make a moderately changing field distribution in a large area.

Figure 19 shows the superimposed shadow images of FIB shaped grid with and without external potential, which is the same as the one used in section 3.2. The applied external voltages to the counter electrode in Fig. 19a and b were 20 V and 10 V, respectively. The averaged shifts of the grid correspond to the external potential as shown by the dotted line arrows in the figures. The narrow and thick line arrows in each figure indicate the unequal shift of the lattice holes from the position of without and with external potential to the electrodes, respectively. In Fig. 19a, there is systematic distortion in the position of the holes, and almost no distortion was observed in Fig. 19b. The carbon film in the metal crescent has been removed during specimen preparation for Fig. 19a. The local non-uniform distribution of electric field is formed in the metal crescent. However, the carbon film in the metal crescent will have the same potential as the metal electrode, which means that there is uniform potential distribution in the area shown in Fig. 19b; therefore, there is no distortion of the shadow of the lattice. This result shows that the rapid change of electric field near the specimen can be detected separately from the moderately changing electric field in the wide area, if the local distortion is taken into account in the hole shift of the shadow image of the lattice. Of cause, the complete separation and quantitative evaluation of the local field requires comparison between numerical calculation and measured value.

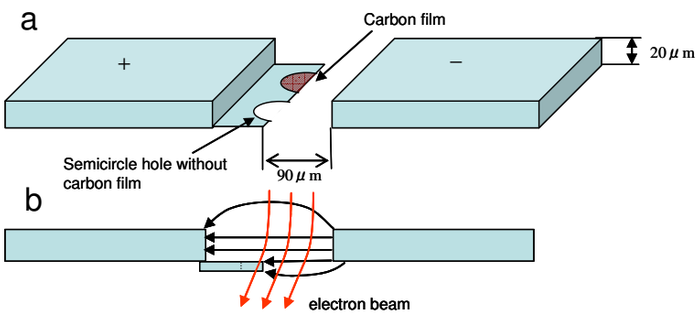

Fig. 18. Schematic drawing of (a) the specimen configuration and (b) the cross sectional view of the specimen. The electric lines of force (arrows of sold line) and the electron beam trajectories (arrows of red line) are drawn, schematically.

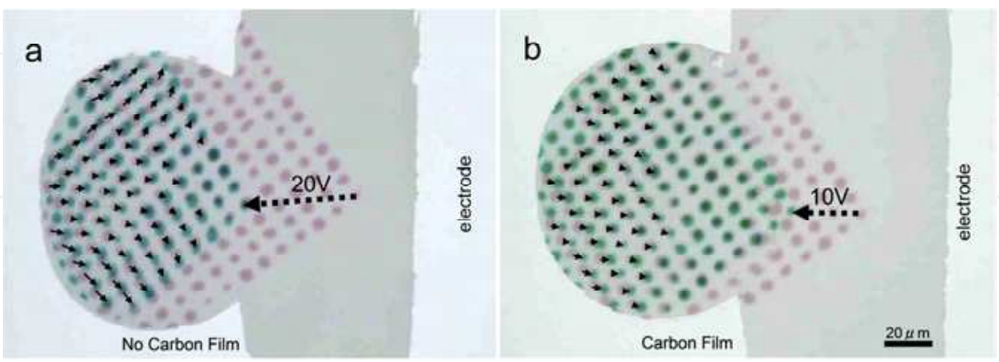

Fig. 19. The 2D-maps showing the difference of the local field distribution in the semicircle holes (a) without and (b) with carbon film indicated by the solid line arrows. The shallow pink and green grids correspond to the shadow image before and after applying potential. The conductive carbon film normalized the field in the hole (b). The whole shifts of the shadow image of the grid (the dotted line arrows) correspond to the field strength in the upper part of the specimen.

4.2 Two-dimensional field distribution observation of the reverse biased p-n junction

The second example is the two-dimensional field distribution around a reverse biased p-n semiconductor junction, which we mentioned in section 1.

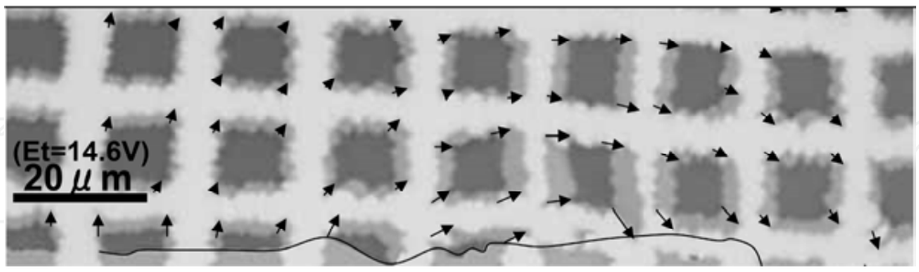

Fig. 20. The electric field observation using the square lattice shaped aperture. The direction and the length of arrows indicate the direction and the strength of the integrated electric field along the electron passage (*Et*). The arrow length of 20 μm in the image corresponds to 14.6 V of *Et*.

Figure 20 shows the shadow image distortion of the square lattice shaped Nickel sheet mesh, which is the superimposition of the shadow image of the lattice without reverse bias onto the image with 5.01 V reverse bias to the specimen. The two images were aligned at a position far enough from the specimen to avoid distortion. The corresponding positions in the two images are connected by arrows. The direction and length of the arrows indicates the direction and strength of the integrated electric field along the electron path (*Et*). The arrows in the figure show the two-dimensional distribution of electric field near the p-n junction in the GaP LED, which is illustrated in Fig. 1. The direction of the field is opposite in the p- and n-regions along the edge of the specimen. In vacuum, a few microns away from the specimen edge, a continuous potential gradient is observed from the p- to the n-region. The result is, qualitatively, in good agreement with the electron holography observation (Sasaki, et. al., 2000; Wang, et al., 2003). At present, the separation of the contribution of the field which is near the specimen from the field away from the specimen is not available, because the detailed numerical calculation of the field around the specimen has not been completed due to the complicated shape of the specimen. The quantitative measurement of this method will be shown in the next subsection.

4.3 Quantitative field distribution measurement around a field emitter needle

The third example is the field distribution around an emitter needle of the field emission electron gun (Sasaki, et al., 2008b; Sasaki, et al 2010). In this system, the materials comprising the specimen are made of metal. The surface potential could be specified almost as the applied potential. Then the numerical calculation would be simpler than the example discussed in the section 4.2.

The two dimensional distribution of the measured value was compared with the calculated value using the surface charge method (Murata, et al., 2004). The numerical calculation model of the specimen was constructed based on the optical image shown in Fig. 21 and TEM observation, though the asymmetry of the needle was not taken into account in the first approximation.

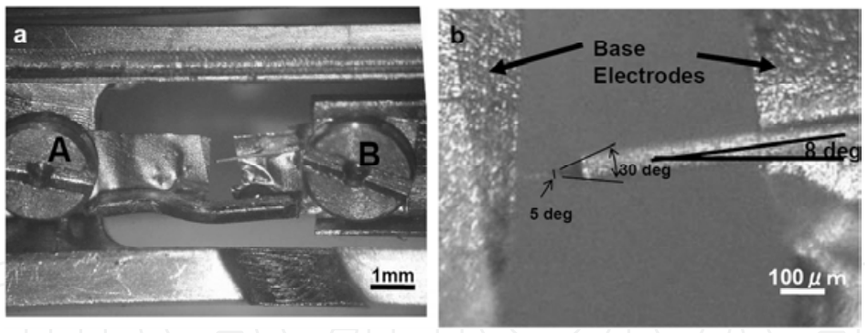

Fig. 21. An optical micrograph of the specimen (a). The enlarged image between the needle tip and the grounded electrode is shown in (b).

In this experiment, two different types of shadow aperture were used. The first one is the holey carbon film Quantifoil R2/2 as shown in Fig. 22a, which was placed at the position of the SAD aperture. This aperture allows us easy identification of the shift of the shadow image of holes by eye. Another type of shadow aperture has been utilized in order to modify the spatial resolution and to allow an automated analysis. The home made carbon film with the rough surface was fixed onto the 200 mesh Cu grid. The surface of the film was decorated by Au deposited to a thickness of about 10 nm. The carbon film showed randomly distributed granular contrast as shown in Fig. 22b. It was hard to identify the distortion of the shadow image of this aperture by eye. However, the dedicated software using the pattern matching method was employed to detect the distortion in the shadow image.

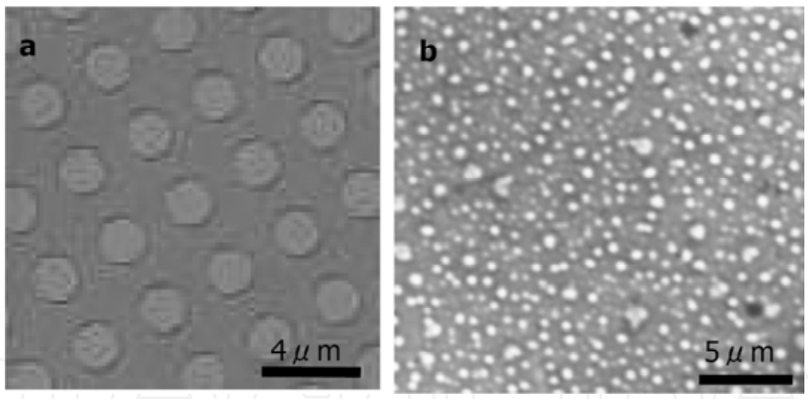

Fig. 22. Two different types of shadow image aperture. (a) Square lattice patterned holy carbon film. (b) Au decorated carbon film with randomly distributed granular contrast.

TEM images of the needle and the shadow images of the Quantifoil R2/2 before applying external voltage and after applying +30 V are shown in Fig. 23a and b, respectively. The shadow image of the aperture is fixed clearly in an area larger than 100 μm×100 μm. In the center of Fig. 23a and b, the image of the needle was observed as a dark shadow because the needle was too thick to be transparent to the electron beam. The square lattice arrangement of the circles corresponds to the shadow image of Quatifoil 2/2. The image of the edge of the ground electrode is seen as the horizontal line in the dark area in the upper part of Fig. 23a and b. The tilted square of dark area surrounding the figures corresponds to the shadow image of the grid mesh which is supporting the holy carbon film of Quatifoil 2/2. There is a discontinuity in the shadow image of the grid mesh at the bottom of the needle in Fig. 23b,

which could be interpreted as the difference of the field direction on the left and right hand side of the needle. The vector of the field on the left and right hand side of the needle has the X part toward left and right hand side, which will shift the shadow image of the grid mesh to left and right hand side, respectively. This counter move of the shadow image causes the discontinuity at the edge of the grid mesh. The images after applying external voltage were superimposed onto the image before applying external voltage carefully aligning the needle images at the same position. The displacement and distortion of the holes of the shadow image of the aperture were observed, particularly near the needle tip in Fig. 23b. The displacement of the shadow image of corresponding holes in the shadow aperture was measured for each hole in the superimposed images. In the measurement, X and Y axes which are parallel and perpendicular to the edge of the ground electrode, respectively, with the origin at the needle tip were determined as shown in Fig. 23a. The displacement *D* was converted to the field strength *Et* using equation (3.5).

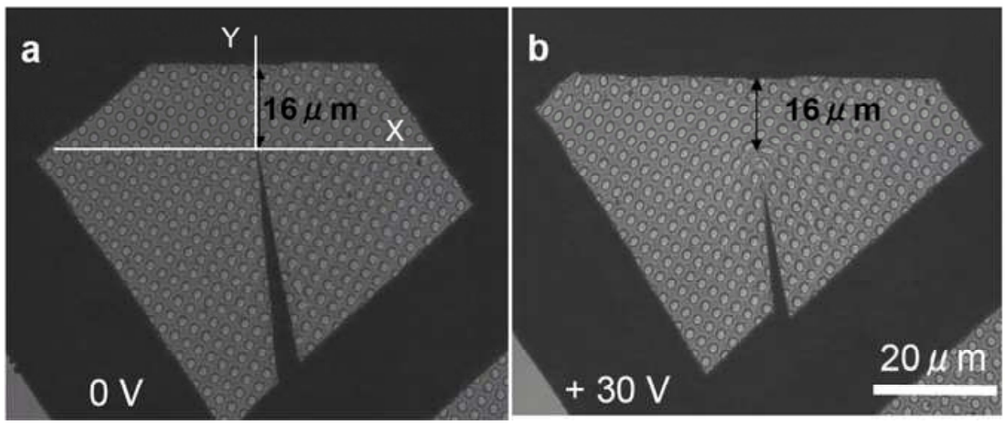

Fig. 23. Shadow images of the Quantifoil R2/2 aperture (a) before and (b) after applying external voltage at +30 V. The displacement and the distortion of the aperture holes are shown in (b).

Figure 24 shows measured values of the electric field at an applied voltage of 30 V. The closed circles in Fig. 24 show the Y component of the electric field, which is perpendicular to the edge of the ground electrode, along the line parallel to the ground electrode as a function of the distance X from the needle. The solid lines in the figure show calculated values using the surface charge method. The calculated values were the integration of the horizontal part of the electric field along the trajectory of the electron above and below the specimen until the value became saturated. The thickness taken into account in the calculation was 2 mm above and below the specimen. Figures 24a, b, c, d, e and f show the Y component of measured and calculated values of the electric field along the line parallel to the ground electrode at Y distance from the tip of the needle for 3 μm, 5 μm, 7 μm, 9 μm, 11 μm and 13 μm, respectively. Due to not only the limitation of the hole position in the shadow aperture but also the tilt of the row of holes to the X axis as shown in Fig. 23, the Y distance measured position could have a repeated systematic increase and sudden decrease of errors in the range of ± 1 μm from the given positions. Such systematic error in the measured position causes a systematic error in field strength of about ± 1 V, which could account for the shallow pseudo shoulder in the field distribution at the discontinuity of error. Taking into account the estimated error, it was found that the measured values showed good agreement with the calculated values with an error of less than 10%. In the

range of this error, the measured value of the field decreases monotonically as a function of the X distance from the needle. However, in Fig. 24f, the dispersion of the value became wider than the estimated error. This is due to the field disturbance caused by the irregularity of the shape of the ground electrode and the charging up of dust at the edge of the electrode, which could be observed by the irregular distortion of the shadow image of holes along the ground electrode in Fig. 23b. The agreement was better on the left hand side of the figures. Particularly in Fig. 24a, a rapid increase of the value near the needle tip showed good agreement with the calculated value. In contrast to the good agreement between the measured and the calculated values on the left hand side, the results on the right hand side in the figures showed comparably poor agreement, perhaps, because of the asymmetry of the field due to the tilt of the needle at an angle of 8 degrees from the line perpendicular to the edge of the ground electrode. Further detailed calculation taking into account the asymmetry of the needle will be required. However, the asymmetry could be understandable qualitatively as follows. When the needle is tilted counter-clockwise as in Fig. 23, the vector of the field will follow the tilt. In the left hand side of the needle, the vector of the field will turn away from the perpendicular line to the ground electrode and then the Y component of the vector will decrease. However, the field attracted to the ground electrode could have the tendency to tilt back to the perpendicular line to the ground electrode, which will reduce the decrease of Y component of the vector. In the right hand side of the needle, the vector of the field will be tilted and positioned along the perpendicular line to the ground electrode, which will increase the Y component of the vector. However, the compensation of the field rotation could not work compared to the left hand side of the needle, and then the increase of the Y component of the vector in right hand side of the needle will remain.

The spatial resolution using the shadow aperture which has a square lattice pattern should be limited by the spacing of the pattern. In order to improve the spatial resolution of the method, a modified shadow aperture which gives the shadow images of randomly dispersed dots and dedicated software which allows automatic detection of the shadow image distortion have been applied to measure the field distribution at the tip of the needle. Figure 25 shows the main window of the developed software. The shadow images before and after applying an external field by applying 4 V to the electrode are shown in Fig. 25a and b. It was hard to identify the difference between the two images by eye. However, the pattern matching method (Szeliski, 2006) revealed the distortion in the shadow image. The image was divided into a series of cell-like images with size SX and SY. The template images were selected with size CX and CY in each cell of the image before applying external voltage. The sum of the squares differences (SSD) was calculated between the template and the corresponding cell-like image after applying external voltage shifting the position up and down to AX and AY. At the minimum of the SSD found in the area of AX and AY, the shift parameters in X and Y direction were determined to be the displacement vector of the template image in the image after applying the external voltage. The displacement vectors were displayed as the solid line which originates at the center of the circle indicating the left upper corner of the template as shown in Fig. 25c. The processed image using this software showed the two-dimensional field distribution with spatial resolution less than 1 μm. In the area where there was no rapid change of the field, the spatial resolution of the software was modified up to 100 nm. However, in the area near the needle tip, the simple SSD function gave the wrong result due to the large distortion in the shadow image. Further modification in the pattern matching method will be required to obtain nanometer spatial resolution without exception.

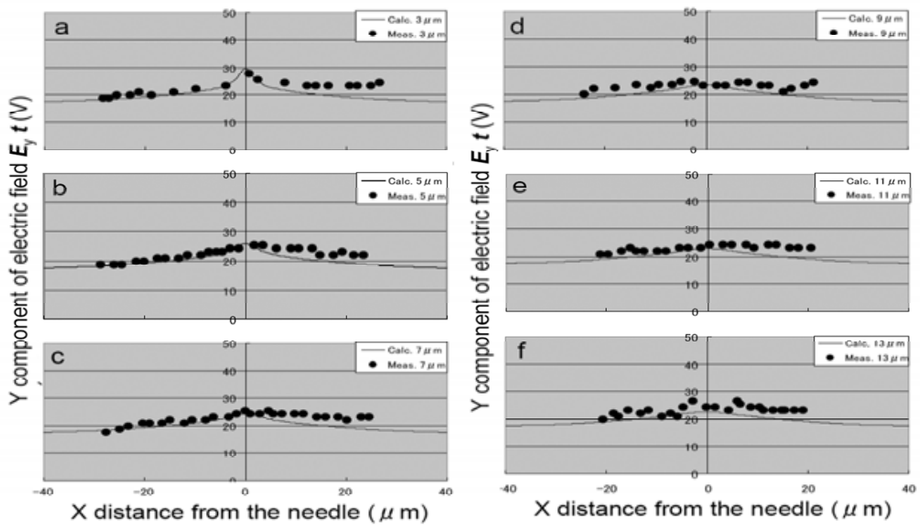

Fig. 24. Y component of the electric field as a function of the distance X from the needle along the line parallel to the ground electrode with distance from the tip of the needle at (a) 3 μm, (b) 5 μm, (c) 7 μm, (d) 9 μm, (e) 11 μm and (f) 13 μm, respectively.

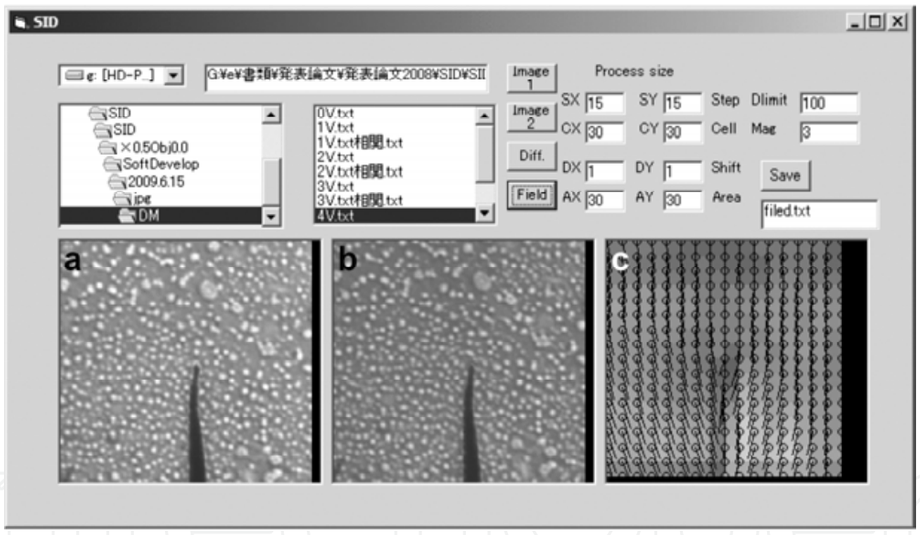

Fig. 25. The main window of the developed software. The shadow image (a) before and (b) after applying external voltage at 4 V, and (c) the detected image distortion corresponding to the electric field distribution.

5. Conclusion

We have developed a simple and quick method to measure the electric and magnetic field around a specimen using a conventional TEM. In this chapter, we have discussed the geometrical optics analysis of our method in a modern conventional transmission electron microscope. The results suggested that the shift of the shadow image of the beam obstructer placed at the position of the selected area diffraction aperture is proportional to the deflection angle around the specimen. It was found that the magnifications of the specimen

image $M_i \times M_p$ and the shadow image of the beam obstructer M_d and M_{ap} on the fluorescent screen have an important role in measuring the electric and magnetic fields at the specimen. The magnification $M_i \times M_p$ can be measured obtaining the lattice image of the specimen with known spacing. The method to evaluate the optical parameters M_d and M_{ap} using the current applied to the second condenser lens and objective lens has been discussed. The quantitative measurement of the electric field has been tested in a uniform field. The comparison of the experimental result with the numerical calculation of a long range field distribution showed the possibility of quantitative measurement of the electric field using this method.

Some preliminary applications have been introduced. Two examples of qualitative observation of the two dimensional projection of the electric field along the electron beam direction were investigated involving a qualitative separation of the field near the specimen from the moderately distributing field away from the specimen.

An example of the quantitative measurement of the electric field has been shown using the electric field distribution at the tip of a narrow needle. The measured value was confirmed as the integrated value of the horizontal part of the electric field along the electron trajectory. The result showed not only good agreement with the calculated value with error of less than 10% but also the possibility to reveal further detail of the electric field distribution. The dedicated shadow aperture and software allow us to map the electric field distribution with spatial resolution on the order of 100 nm, particularly in the area where the field is changing moderately. We believe that the method can measure the two-dimensional distribution of the field over an area more than 100 μm with submicron spatial resolution.

Our method is limited to the LM mode. However, it is possible to detect the electromagnetic field distribution in a large area at the specimen level, since the method simply detects the deflection of the electron beam at that level. As shown in section 3, the electromagnetic field is usually distributed over a wide area in and/or around the specimen. In electron holography, the reference electron wave will be affected by the electromagnetic field in the region that it is traversing, whereas the interference region in the image of an electron hologram is limited to a bundle like shape. Our method can also be performed in a field emission gun transmission electron microscope (FEG-TEM) equipped with an electron bi-prism because the electron bi-prism is placed at the same position as where the SAD aperture was placed. The distortion of the shadow image of the bi-prism had been observed in an electron holography observation (Sasaki, et al., 2000). The narrow and sharp image of the bi-prism is more suitable than the irregular edge shape of the SAD aperture for quantitative measurements. Similar phenomenon has been studied by Pozzi (1975, 1980 and 1982) and Frzzini et al., (2006). In order to estimate and/or correct the phase disturbance in the reference wave of electron holography, using both methods simultaneously would be advantageous.

The Lorentz microscopy uses contrast modification of the specimen image due to the field. Therefore, it cannot obtain any information in the area of vacuum. Our method is suitable to observe the field distribution in vacuum rather than in the material which reduces the intensity of the electron beam. Simultaneous use of both methods could make them complementary to each other.

Some other shadow methods (Marton and Lachenbruch, 1949; Jakubovics, 1964; Ishba et al., 1974) which have optics similar of the Foucault mode of Lorentz microscopy, i.e., the beam obstructer is placed after the imaging lens, have already been developed, however, the methods have never been used in a wide variety of applications. Presumably, the optics has a problem, because the imaging lens which has the strongest magnetic field will be changed and adjusted during imaging in these methods. This causes a change of major optics parameter, which gives instability to the optics and a loss in quantitative ability of the measurement. Our method avoids this problem by using the 1st intermediate lens as an imaging lens, which is placed after the beam obstructer.

In future development, observation of the field distribution inside materials will be required, and employment of the HVEM looks promising. Improvement of the spatial resolution in a medium voltage electron microscope to better than 10 nm has been obtained through higher magnification (Mori, 2009). Though the complete quantitative comparison with other methods, for example, electron holography (Oikawa et al. 2007), will be required to generalize this method, we can foresee that our method will give more fluent results, not only if it is used with other methods, i.e., electron hologram or the Lorentz microscopy but also as a standalone method .

6. Acknowledgement

This work was supported by Grants-in-Aid for Scientific Research B18360303 and B21360307.

7. References

Bajit, S., Barty, A., Nugent, K. A., McCartney, M., Wall, M. and Paganin, D., (2000). Quantitative phase-sensitive imaging in a transmission electron microscope. *Ultramicroscopy*, 83, pp. 67-73.

Blackman, M. and Grunbaum, E (1957). An investigation into the effect of magnetic domains in cobalt on an electron beam. *Proc. Roy. Soc.* A241, pp. 508-521.

Cohen, M., (1968) Recent developments in Lorentz electron microscopy. *IEEE Trans. Mag.*, MAG4, 1, pp. 48-50.

Chapman, J. N., (1984). The investigation of magnetic domain structures in thin foils by electron microscopy. *J. Phys.*, D17, pp. 623-647.

Fisher, R. D., and Blades, J. D., (1972). Recording gap fields by Lorentz shadowgraphs and characteristics of single crystal MnZn ferrites. *IEEE Trans. Mag.*, MAG8, 2, pp. 232-238.

Frzzini, P. F., Ortolani, L., Pozzi, G. And Ubaldi, F., (2006). Interference electron micrography of one-dimensional electron-optical phase objects. *Ultramicrocsopy*, 106, pp. 620-629.

Graef, M. De. and Zhu, Y., (2001). Quantitative noninterferometric Lorentz microscopy. *J Appl. Phys.*, 89, pp. 7177-7179.

Ishba, T., and Suzuki, H., (1974). Measurements of magnetic field of magnetic recording head by a scanning electron microscope. Jpn. J. Appl. Phys., 13, 3, pp. 457-462.

Jakubovics, J. P., (1964). The effect of flux closure at the edges of thin cobalt films on electron microscope images. *Philos. Mag.* 10, pp. 675-694.

Kamino, T. and Saka, H., (1993). Newly developed high resolution hot stage and its application to material science. *Microsc. Microanal. Microstruct.*, 4, pp. 127-135.

Keyser, U., Schaerpf, O and Schwink, Ch., (1975). Electron optic investigation of magnetic stray field on (110) planes of Ni crystals oriented with high accuracy. *Physica* 80B, pp. 389-396.

Lazzari, J. P. and Wade, R. H., (1971). Electron probe measurements of field distributions near magnetic recording heads. *IEEE Trans. Mag.*, MAG7, pp. 709-704.

Marton, L. and Lachenbruch, H., (1949). Electron optical mapping of electromagnetic fields. *J. Appl. Phys.* 20, pp. 1171-1182.

Merli, P. G., Missiroli, G. F. and Pozzi, G.. (1975). *Phys. Stat. Sol.*, A30, pp. 699-711.

Mori, H., (2009). *Master thesis*, Nagoya University, Nagoya, Japan (in Japanese).

Murata, H., Ohye, T., and Shimoyama, H., (2004). High accuracy calculation of electric field in composite dielectric system by improved 3-D boundary charge method. *Nucl. Inst. Meth. Phys. Res.*, A519 pp. 184–195.

Oikawa, T., Kim, J. J., Tomita, T., Park, H. S., and Shindo, D., (2007). Measurement of electric potential distributions around FEG-emitters by electron holography. J. Electr. Microsc. , 56, 5, pp. 171-175.

Pozzi, G., and Vanzi, M., (1982). Interpretation of electron interference images of reverse-biased p-n junctions. *Optic*, 60, 2 pp. 175-180.

Pozzi, G., (1980). Asymptotic approximation of the image wavefunction in interference electron microscopy. II. Extension to the biprism edges. Optic, 56, 3, pp. 243-250.

Pozzi, G., (1975). Asymptotic approximation of the image wavefunction in interference electron microscopy. Optic, 42, 1, pp. 97-102.

Sasaki K, Kato N, Miyashita K, Wang Z, Hirayama T, Saka H. (2000). Development of FIB Techniques for the *In-Situ* Observation of Living Semiconductor Devices. *Electron Microscopy*, 35 Supplment 1, p. 190.

Sasaki, K., Wang, Z., Hirayama, T., Yaguuchi, Y., Saka H. (2003). Electron holography observation of p-n junction in a semiconductor. *Electron Microscopy*, 38, pp. 216-218 (in Japanese).

Sasaki, K., and Saka, H., (2005). A Simple method of the electric/magnetic field observation by a conventional transmission electron microscope. In: *Materials Science Forum 475-479*, Zhong, Z. Y., Saka, H., Kim, T. H., Holm, E. A., Han, Y. F. and Xie, X. S., Trans Tec Pub., Zurich, pp. 4029-4034.

Sasaki, K., Wang, Z., Fukunaga, K., Hirayama, T., Kuroda, K. and Saka, H., (2006). In-Situ TEM Observation of Electromagnetic Field in Some Real Materials. Materials Research Society Symposium Proceedings 907E, 0907-MM04-02, pp. 1-6, Boston, USA, Dec., 2006.

Sasaki, K., Kubo, Y. and Kuroda, K., (2008a). Shadow Image Distortion in a Conventional Transmission Electron Microscope. *Korean Journal of Microscopy* 38, Supplement, pp. 33-34.

Sasaki, K., Tanaka, N., Murata, H., Morita, C., Shimoyama, H. and Kuroda, K., (2008b). Electric Field Observation around a FEG-Emitter Tip Using a Conventional TEM. *Int. J. Adv. Microsc. Theor. Calc. Lett* 1 pp. 98-99.

Sasaki, K., Mori, H., Tanaka, N., Murata, H., Morita, C., Shimoyama, H. and Kuroda, K., (2010). Measurement of electric field distribution using a conventional transmission electron microscope. *J. Electr. Microsc.*, 59, pp. S89-S94.

Szeliski, R., (2006). Image Alignment and Stitching. In: *Handbook of Mathematical Models in Computer Vision*, Paragios N, Chen Y and Faugeras O, pp. (273-292), Springer, New York.

Tonomura, A., (1987). Applications of electron holography. *Rev. Mod. Phys*., 59, pp. 639-669.

Wade, R. H., (1976). The measurement of magnetic microfields. *IEEE Trans. Mag*., MAG12, pp. 34-38.

Wang, Z., Kato, N., Sasaki, K., Hirayama, T. and Saka, H., (2004). Electron holographic mapping of two-dimensional doping areas in cross-sectional device specimens prepared by the lift-out technique based on a focused ion beam. *J. Electr. Mmicrosc.* 53, pp. 115-119.

Wang, Z., Sasaki, K., Hirayama, T., Yabuuchi, Y. and Saka, H., (2003). Observing a p-n junction in a reverse-biased GaP light-emitting diode by combining electron holography and focused-ion-beam milling. *Microsc. Microanal*., 9, supplement, pp. 772-773 .

Williams, D. B. and Carter, C. B., (1996). *Transmission Electron Microscopy, Basics I*. Plenum Press, New York, p. 1356

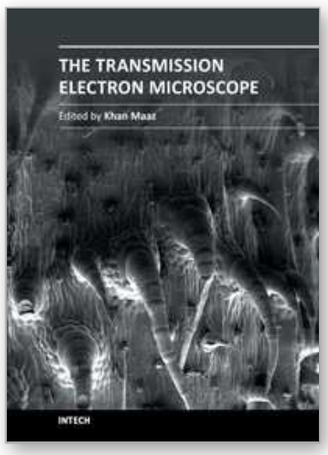

The Transmission Electron Microscope

Edited by Dr. Khan Maaz

ISBN 978-953-51-0450-6
Hard cover, 392 pages
Publisher InTech
Published online 04, April, 2012
Published in print edition April, 2012

The book "The Transmission Electron Microscope" contains a collection of research articles submitted by engineers and scientists to present an overview of different aspects of TEM from the basic mechanisms and diagnosis to the latest advancements in the field. The book presents descriptions of electron microscopy, models for improved sample sizing and handling, new methods of image projection, and experimental methodologies for nanomaterials studies. The selection of chapters focuses on transmission electron microscopy used in material characterization, with special emphasis on both the theoretical and experimental aspect of modern electron microscopy techniques. I believe that a broad range of readers, such as students, scientists and engineers will benefit from this book.

INTECH
open science | open minds

InTech Europe
University Campus STeP Ri
Slavka Krautzeka 83/A
51000 Rijeka, Croatia
Phone: +385 (51) 770 447
Fax: +385 (51) 686 166
www.intechopen.com

InTech China
Unit 405, Office Block, Hotel Equatorial Shanghai
No.65, Yan An Road (West), Shanghai, 200040, China
中国上海市延安西路65号上海国际贵都大饭店办公楼405单元
Phone: +86-21-62489820
Fax: +86-21-62489821

IntechOpen